

Polarimetric observations of OH masers in proto-planetary nebulae[★]

M. Szymczak¹ and E. Gérard²

¹ Toruń Centre for Astronomy, Nicolaus Copernicus University, Gagarina 11, 87-100 Toruń, Poland
e-mail: msz@astro.uni.torun.pl

² GEPI, UMR 8111, Observatoire de Paris, 5 place J. Janssen, 92195 Meudon Cedex, France

Received 17 March 2004 / Accepted 28 April 2004

Abstract. The 1612 and 1667 MHz OH maser lines have been measured in all four Stokes parameters in 47 proto-planetary nebula (PPN) candidates. Out of 42 objects detected, 40 and 34 are 1612 and 1667 MHz emitters, respectively. The spectral extent of the 1667 MHz line overshoots that of the 1612 MHz line in about 80% of the targets. 52% and 26% of the 1612 and 1667 MHz sources, respectively, show linear polarization in at least some features. Circular polarization is more frequent, occurring in 78% and 32% of sources of the respective OH lines. The percentage polarization is usually small (<15%) reaching up to 50–80% in a few sources. Features of linearly polarized emission are usually weak (0.5–4 Jy) and narrow (0.3–0.5 km s⁻¹). The strength of the magnetic field inferred from likely Zeeman pairs in two sources of a few mG is consistent with values reported elsewhere for those classes of objects. An upper limit of the electron density in the envelope of OH17.7–2.0 derived from the difference in the position angle of polarization vectors for the two OH lines is about 1 cm⁻³. Distinct profiles of polarization position angle at 1612 and 1667 MHz are seen in about one third of the sources and strongly suggest that the envelopes are permeated by structured magnetic fields. The geometry of the magnetic field is implicated as an important cause of the depolarization found in some PPN candidates. For the subset of targets which show axisymmetric shells in the optical or radio images we found a dominance of magnetic field components which are orthogonal to the long axis of the nebulae. This finding supports the hypothesis that such bipolar lobes are shaped by the magnetic field.

Key words. polarization – masers – stars: AGB and post-AGB – ISM: planetary nebulae: general – stars: circumstellar matter

1. Introduction

It has been recognized that at the end of their lives on the asymptotic giant branch (AGB), low- and intermediate-mass stars (1–8 M_{\odot}) experience intense mass loss at rates of more than $10^{-5} M_{\odot} \text{ yr}^{-1}$ (Habing 1996, for a review). This results in slowly expanding molecular circumstellar envelopes which can produce strong maser lines. During about 10^3 yr after cessation of mass loss, stars evolve through a transitional proto-planetary nebula (PPN) phase into planetary nebulae (PNe). In the PPN phase an extensive dust-gas envelope can enshroud a cool ($\leq 10^4$ K) post-AGB stellar core while the photoionization of circumstellar matter is not yet initiated (Kwok 1993). It is thought that somewhere during the PPN phase, the envelope must depart from the high degree of spherical symmetry seen in most AGB stars to a variety of axisymmetric structures observed in most PNe (Ueta et al. 2000). Possible causes of the axisymmetric morphology of such outflows are generally attributed to: 1) the interaction of a fast post-AGB stellar wind ($\geq 10^3$ km s⁻¹) with a slow AGB wind with an equatorial density enhancement; 2) the effect of the gravitational field of a

binary companion and 3) the dynamic effect of the progenitor magnetic field (Balick & Frank 2002, for a review).

The role of the magnetic field in the shaping of PPN has recently received considerable attention. Chevalier & Luo (1994) proposed the magnetized wind-blown bubble model in which initially weak toroidal magnetic fields carried in a fast wind are strengthened and produce prolate and bipolar structures (e.g., Garcia-Segura et al. 1999; Matt et al. 2000). Soker (2002) argued that the magnetic field does not play a global role in the shaping of PPN but that the locally strong magnetic field may facilitate the maser amplification.

The presence of magnetic fields around AGB and late type stars has been proved by maser polarization studies (e.g., Kemball & Diamond 1997; Szymczak & Cohen 1997; Szymczak et al. 1998, 2001; Bains et al. 2003a). OH maser emission appears to be the best tracer of magnetic fields in the outer circumstellar regions providing information on the direction, strength and orientation of the fields.

OH masers have been found in several PPN candidates during the surveys of very cold IRAS sources (Likkell 1989; te Lintel Hekkert 1991; Hu et al. 1994; te Lintel Hekkert & Chapman 1996) and of radio continuum sources or young PNe (Zijlstra et al. 1989). Some PPN candidates with OH emission

[★] Figures in Appendix are only available in electronic form at <http://www.edpsciences.org>

were identified on the basis of their irregular spectra with a velocity range over 50 km s^{-1} (Zijlstra et al. 2001). Polarization properties of OH masers associated with PPNe are poorly known. Zijlstra et al. (1989) measured the circular polarization in 5 objects and a high percentage polarization ($>80\%$) was found in IRAS 17150–3754 at 1612 MHz. Another object with strongly circularly polarized emission in all OH lines was IRAS 16342–3814 (te Lintel Hekkert & Chapman 1996). Miranda et al. (2001) reported that the PPN K3-35 shows strong circular polarization at 1667 MHz. However, nothing is known about the linear polarization of OH masers in PPNe.

In this study we describe the results of a full polarization survey of OH masers in 47 PPN candidates. With the full polarization data we wish to better understand the properties of the circumstellar material of PPNe and to see if there is evidence that the magnetic field can facilitate the development of axisymmetric morphology. Our data should help to choose the best candidates for mapping the magnetic fields with the aperture synthesis technique. This paper provides the first evidence for the dominance of the magnetic field components perpendicular to the long axis of proto-planetary nebula.

2. Observations

The 1612 and 1667 MHz lines of OH were observed with the upgraded Nançay Radio Telescope (NRT) (van Driel et al. 1996) in a series of observing runs between February 2002 and June 2003. At the OH frequencies, the half-power beam-width of the telescope is $3'5$ in the E–W direction and $19'$ in the N–S direction. At $\delta = 0^\circ$, the beam efficiency is 0.65 and the point source efficiency is 1.4 K Jy^{-1} . The system temperature is about 35 K.

The new focal system of the NRT consists of a dual-reflector offset Gregorian configuration fed by a corrugated horn. The horn itself is followed by an ortho-mode transducer providing two linear orthogonal polarizations. The feed box can be rotated, with a precision of 0.5° , at any angle between from -90° to $+90^\circ$ from a rest position of 0° (where the position angles of the electric vectors are 45° and 135°). The maximum level of the cross-polarization lobe is -22 dB . The linearly polarized signals are then up-converted, equalized in amplitude and phase and combined in a 7 GHz hybrid to yield right hand (RHC) and left hand (LHC) circularly polarized signals. The isolation of opposite circular polarizations is better than 20 dB. The signals of the four RF channels (the two linear polarizations without hybridization and the two circular polarizations) are then down converted and the four IF channels transported to the laboratory. This system directly provides 3 of the 4 Stokes parameters namely I , Q and V while the fourth parameter U is readily obtained by rotating the feed box by 45° as is apparent from Eqs. (2) and (3) below. The gain of each polarization channel was measured with a noise diode at the beginning of each 3 min integration scan to $\sim 5\%$ in absolute value and to within $\sim 1\%$ in relative value.

A 8192 channel autocorrelator configured into eight banks of 1024 channels was used as spectrometer. The two OH transitions were simultaneously observed with a spectral resolution of 0.07 or 0.14 km s^{-1} . For a few sources, with an OH maser

spectral extent greater than 60 km s^{-1} , the data were taken with a resolution of 0.28 km s^{-1} . The radial velocities were measured with respect to the local standard of rest. The two orthogonal linear polarizations and two opposite circular polarizations of each OH line were observed at feed box positions of 0 and 45° .

The typical integration time for each feed box position was about 20 min. The calibration of the instrumental polarization and of the polarization position angle was verified with regular observations of W3OH and OH17.7-2.0. The polarization characteristics of those secondary calibrators are known from interferometric observations (Garcia-Barreto et al. 1988; Bains et al. 2003a). Moreover, the percentage of linear polarization and the position angle (PA, measured eastward from north) of the electric vector of the continuum source 3C286 were measured at 1400 MHz and found to be $8.5 \pm 0.5\%$ and 33 ± 0.3 , respectively (Colom, private communication), in good agreement with published values (Bridle et al. 1972).

The four Stokes parameters were calculated for each velocity channel using the following equations:

$$I = S(0) + S(90) = S(\text{RHC}) + S(\text{LHC}) \quad (1)$$

$$Q = S(0) - S(90) \quad (2)$$

$$U = S(45) - S(-45) \quad (3)$$

$$V = S(\text{RHC}) - S(\text{LHC}), \quad (4)$$

where $S(0)$, $S(90)$, $S(45)$ and $S(-45)$ are the line flux density at PAs of 0° , 90° , 45° and -45° , respectively. $S(\text{RHC})$ and $S(\text{LHC})$ are the line flux densities for right and left circular polarizations, respectively. The linearly polarized flux density $p = \sqrt{Q^2 + U^2}$, fractional linear polarization $m_L = p/I$, fractional circular polarization $m_C = V/I$ and polarization position angle $\chi = 0.5 \cdot \tan^{-1}(U/Q)$ were derived from the Stokes spectra. The uncertainties in the fractional linear polarization and the polarization position angle (McIntosh & Predmore 1993) are

$$\sigma_{m_L} = \left(\sqrt{p^2 \sigma_I^2 / I^2 + \sigma_Q^2} \right) / I \quad (5)$$

and

$$\sigma_\chi = \sigma_Q / \sqrt{2}p, \quad (6)$$

where σ_I , σ_Q and σ_p are the rms noises of the I , Q and p spectra, respectively. As discussed by Wardle & Kronberg (1974), the non-Gaussian probability distribution of the polarized electric vector may lead to systematic errors when the signal-to-noise ratio (SNR) is small. We have neglected this effect since we only considered emission features with a SNR greater than 5.

A typical σ_I was about 35 mJy for 0.14 km s^{-1} spectral resolution. Baseline subtraction was done by frequency switching. This mode introduces an error of less than 0.6% in the polarization parameters, as compared to the position switching mode. No correction for ionospheric Faraday rotation was applied to the data. The absolute uncertainty of the OH polarization measurements is less than 7%.

Each target was observed 3–5 times on an irregular basis to check the quality of polarization data rather than to study the variability, which is beyond the scope of this paper. Consistent polarization parameter measurements were obtained for all objects at epochs spanning 3–15 months. Data for one epoch are presented and analyzed here with the exception of Sect. 5.3 where data from 2–5 observations are used to derive the polarization position angles. This procedure is of special value for sources with weak p flux to improve the accuracy of polarization position angle estimates.

3. The sample

We selected 47 target sources from several surveys of OH masers of IRAS sources with dust temperatures between ~ 100 K and ~ 200 K. This range is typical for late AGB stars and early post-AGB heavily obscured by thick circumstellar envelopes only detectable in the infrared, as well as for post-AGB and young PN still associated with the infrared emission but with optically visible central stars of spectral types from M to B (Likkell 1989; Zijlstra et al. 1989; te Lintel Hekkert 1991; Hu et al. 1994; te Lintel Hekkert & Chapman 1996; Zijlstra et al. 2001). OH maser emission from those objects at one or more transitions is usually over 50 km s^{-1} wide and significantly different from the conventional standard twin-peaked AGB star OH1612-MHz maser profile. Sometimes the red-shifted peaks are weak or absent. Some objects with a moderate OH velocity range of $20\text{--}30 \text{ km s}^{-1}$ are included because they have been revealed as bipolar nebulae by radio observations (e.g. W43A, K3-35). Our sample also contains some objects detected as OH masers during the surveys of known young PN or radio continuum sources (Zijlstra et al. 1989). We did not include PPN candidates lying in directions of strong background OH confusion where the genuine OH emission of the source cannot be unambiguously resolved with the telescope beam. The well-known OH supergiant stars with high outflow velocities are excluded from our list. The sample is confined to the objects with $\delta > -39^\circ$.

4. Results

Table 1 lists the objects observed and contains velocity ranges (ΔV) and integrated flux densities (S_i) at 1612 and 1667 MHz. For sources with only the blue- or red-shifted emission detected the measured values of ΔV are denoted by asterisks while the presumed values of ΔV , discussed below in Sect. 4.6, are given in italics. For the non-detections we list the 3σ noise levels.

Figure 1 shows the 1612 MHz polarization spectra of OH17.7–2.0. Circularly and linearly polarized emission was detected in the blue- and red-shifted parts of the spectrum. The percentage of linear and circular polarization was generally lower than 8% and $\pm 15\%$, respectively. We note that changes in the PA of linear polarization across the spectrum closely follow the pattern observed with MERLIN (Bains et al. 2003a). This result demonstrates that the NRT spectrum provides a reliable measure of the magnetic field orientation in this circumstellar envelope the structure of which was resolved

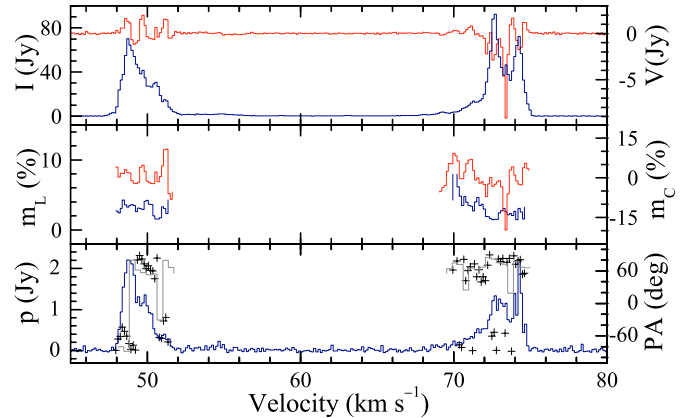


Fig. 1. Polarization spectra for the 1612 MHz transition in IRAS 18276–1431 (OH17.7–2.0) taken on 2002 February 20. *Upper panel:* the total flux (I Stokes) (black/blue line) and the circularly polarized flux (V Stokes) (grey/red line); *middle panel:* the percentage linear polarization (m_L) (black/blue line) and the percentage circular polarization (m_C) (black/blue line); *lower panel:* the linearly polarized flux ($p = \sqrt{Q^2 + U^2}$ Stokes) (black/blue line) and the position angle (PA) of the polarization vector (crosses). The grey/red line in the lower panel shows the flux-weighted PA of polarization vector observed with MERLIN on 1999 May 19 (Bains et al. 2003a).

with a $0''.2$ beam. Furthermore, it suggests that the field orientation is stable over a period of about 2.5 years. Because our data were taken with a spectral resolution of a factor of 2.6 higher than that of MERLIN but with a sensitivity about a factor of 4.5 lower, the PA profile is noisier than that deduced from Bains et al. (2003a).

The polarization spectra for the remaining sources for which the p spectra contain at least one feature with $SNR > 5$ are shown in Fig. A.1.

4.1. Polarization statistics

Among the 42 objects detected, there are 32 objects with polarized (circular and/or linear) emission in at least one OH transition (Table 2). 23 sources show linearly polarized emission in either or both of the OH lines. Linearly polarized emission is always associated with circularly polarized emission. 10 out of 31 polarized objects at 1612 MHz show only circular polarization (Table 2). There is a higher probability of detecting linear polarization in the 1612 MHz line (21/40) than in the 1667 MHz line (9/34) (Tables 1 and 2).

The distribution of source counts versus integrated flux density (Fig. 2) demonstrates that polarized emission preferentially occurs in objects with strong emission; at 1612 MHz the average values of S_i in polarized and non-polarized sources are 19.4 and 2.3 Jy km s^{-1} , respectively, whereas at 1667 MHz the corresponding values are 16.7 and 1.1 Jy km s^{-1} . Plot of $|V|$ and p fluxes versus the total flux I of the strongest peak for the whole sample (Fig. 3) clearly shows that only one source with flux less than 0.8 Jy had detectable polarization. Below a flux density of about 2 Jy the polarized source counts are likely to be incomplete.

Table 1. The sample of OH PPN candidates.

IRAS name	Other name	Epoch (JD-2 450 000)	Spectral resolution (km s ⁻¹)	1612 MHz		1667 MHz	
				ΔV (km s ⁻¹)	S_i (Jy km s ⁻¹)	ΔV (km s ⁻¹)	S_i (Jy km s ⁻¹)
06530-0213		2411	0.14		<0.06		<0.05
07331+0021		2461	0.07	10.2	11.6	4.5*(10.9)	0.07
07399-1435	OH231.8+4.2	2442	0.28	32.0	3.2	101.5	179.5
08005-2356		2410	0.28	106.0	3.0	4.0*(111.1)	0.2
16342-3814	OH344.1+5.8	2758	0.14	132.0	33.6	117.0	26.3
16559-2957		2432	0.14		<0.14		<0.09
17079-3844		2502	0.07		<0.13		<0.11
17103-3702	NGC 6302	2602	0.14	21.0*	5.6	10.0 ¹	0.5
17150-3754	OH349.4-0.2	2769	0.14	6.0*	1.1	33.0*	10.4
17150-3224	OH353.8+3.0	2718	0.14	2.8*(28.5)	4.2	31.5	53.9
17233-2602	OH0.1+5.1	2495	0.14	17.7	7.3		<0.11
17253-2831		2370	0.14	31.8	31.6		<0.10
17347-3139		2314	0.14	127.0	5.1	11.0 ²	0.3
17371-2747		2502	0.14	18.2*	11.6		<0.10
17375-2759		2818	0.14	15.6*	5.7	13.8*	1.4
17375-3000		2602	0.14	44.4	11.6	24.4	0.6
17385-3332	OH355.6-1.7	2530	0.28	25.7	18.5	22.4	0.4
17393-2727	OH0.9+1.3	2672	0.07	32.1	199.2	8.2*(34.2)	1.3
17393-3004		2821	0.07	62.5	30.7	38.0 ³	2.9
17404-2713	OH1.2+1.3	2672	0.14	29.2	24.8	30.5	2.7
17423-1755	HEN3-1475	2327	0.28	(24.3)	0.2	54.0	3.6
17433-1750		2628	0.28	32.0	3.4	31.8	0.3
17436+5003	HD 161796	2383	0.07		<0.12		<0.10
17443-2949		2820	0.14	24.8 ⁴	3.5	31.5 ⁵	3.9
17516-2525		2432	0.14	37.2	9.4	37.2	0.8
17579-3121		2683	0.14	24.1	47.6	49.5	0.9
18016-2743		2419	0.14	24.8	3.5		<0.12
18025-3906		2558	0.14	51.6	41.0		<0.23
18052-2016	OH10.1-0.1	2434	0.14	63.0	17.0		<0.14
18071-1727	OH12.8+0.9	2421	0.07	22.3	8.1	23.7	1.2
18091-1815		2436	0.28	32.9	16.8	34.0 ⁶	1.1
18095+2704	OH53.8+20.2	2440	0.14	20.8	0.4		<0.11
18105-1935		2442	0.14	21.8	8.5	25.5	0.6
18135-1456	OH15.7+0.8	2694	0.07	31.3	156.6	32.2	13.5
18266-1239	OH19.2-1.0	2499	0.14	37.7	76.2	38.0	0.6
18276-1431	OH17.7-2.0	2326	0.14	28.0	299.2	28.4	13.2
18450-0148	W43A	2777	0.14	16.2	37.9	19.2	8.6
18491-0207		2421	0.28		<0.20	132.0	37.4
18596+0315	OH37.1-0.8	2430	0.14	30.1	39.0	31.5	1.2
19067+0811	OH42.3-0.1	2694	0.14	35.3	74.3	3*(35.5)	0.2
19114+0002	HD 179821	2809	0.28	55.3	297.5	58.8	184.9
19127+1717		2438	0.14		<0.17		<0.12
19219+0947	VY2-2	2775	0.07	8.5*	19.5		<0.10
19255+2123	K3-35	2420	0.07	25.4	3.4	5.6*	0.2
19343+2926	M1-92	2421	0.14	4.0*(45.8)	0.4	46.0	7.9
22036+5306		2335	0.28	60.7	14.7	66.5	9.0
23321+6545		2447	0.14		<0.14	20.7	0.3

* Width of single feature or complex; Absorption features: ¹ -0.1 Jy at -37.8 km s⁻¹, ² -0.2 Jy at -7.2 km s⁻¹, ³ -0.4 Jy at 1.2 km s⁻¹, ⁴ -0.1 Jy at 4.8 km s⁻¹, ⁵ -0.1 Jy at 4.8 km s⁻¹, ⁶ -0.1 Jy at 30.7 km s⁻¹.

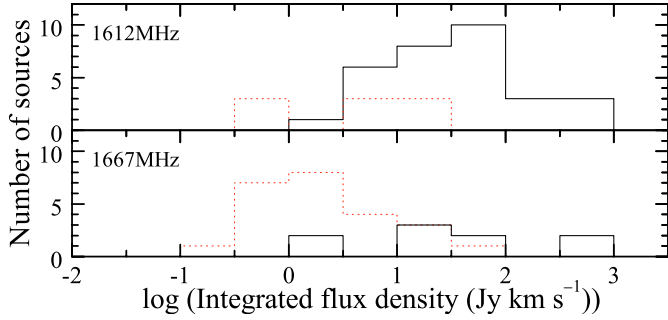


Fig. 2. Histograms of the integrated flux density for sources with polarized (solid line) and non-polarized (dashed line) OH emission.

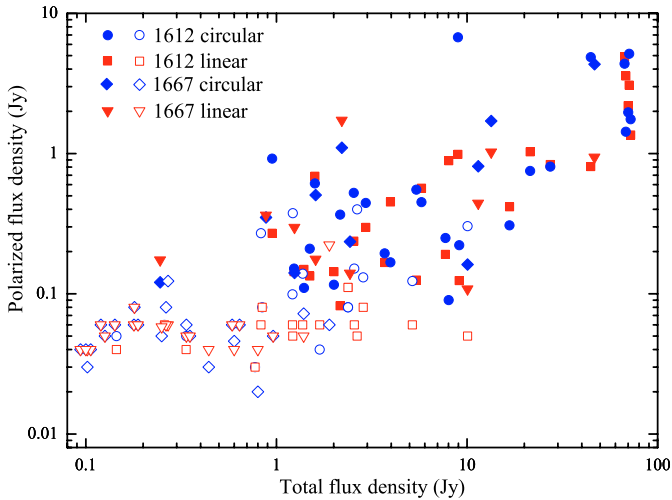


Fig. 3. Polarized flux densities ($|V|$ and p) plotted against the total I flux densities. The filled symbols show sources with linearly (grey/red) and circularly (black/blue) polarized features. The open symbols show sources with only an upper limit for polarized emission.

4.2. Strongly polarized sources

There are 7 OH PPN candidates in the sample with strongly polarized features (Table 2 and Fig. A.1). The most prominent is IRAS 16342–3814 containing, in the blue-shifted part of the 1612 MHz spectrum, several polarized features with $|m_C| > 70\%$ and $m_L = 14\%$. The 1612 MHz features of IRAS 19255+2123 have even higher polarization percentages ($|m_C| > 80\%$, $m_L = 40\%$). IRAS 08005–2356 shows considerable polarization at 1612 MHz ($|m_C| = 37\%$, $m_L = 51\%$) near -0.3 km s^{-1} . In the 1612 MHz line strong circular polarization ($|m_C| = 84\%$) without detectable linear polarization is seen in IRAS 17150–3754, while in IRAS 19067+0811 strong linear polarization of $m_L = 70\%$ is associated with only weak circular polarization ($m_C = 2.1\%$). The 1667 MHz emission of IRAS 18091–1815 and IRAS 18276–1431 is characterized by considerable linear polarization ($m_L = 54\%$). We note that these features with a high degree of polarization are usually weak in total intensity ($< 2 \text{ Jy}$).

4.3. Evidence for complex magnetic fields

The data for OH17.7–2.0 (Fig. 1) indicate that the measurements of the position angles of polarization vectors are fully

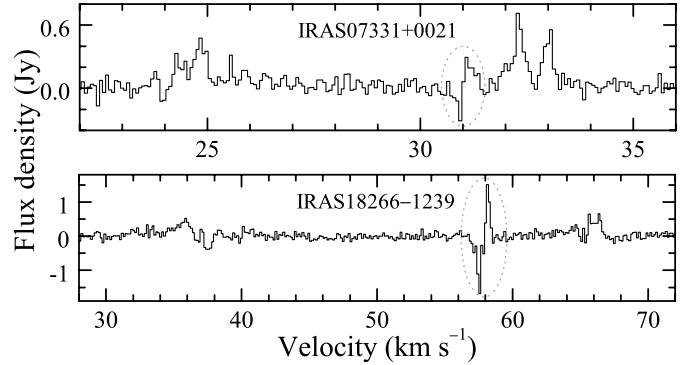


Fig. 4. V Stokes 1612 MHz OH spectra of PPN candidates with possible Zeeman splitting marked by dashed ovals.

consistent with those obtained using an interferometric array. In this source, a large-scale regular magnetic field structure was revealed by Bains et al. (2003a). It is possible that sources with considerable changes in χ across the p profile have structured magnetic fields. In our sample the source IRAS 17393–2727 appears as the best candidate to map a complex magnetic field; a p flux density higher than 1 Jy is seen over a velocity extent of greater than 6 km s^{-1} , χ varies in a characteristic way from -90° to 90° (Fig. A.1). Two further objects, IRAS 07399–1435 at 1667 MHz and IRAS 19067+0811 at 1612 MHz, with linearly polarized flux densities of about 1 Jy, could also have structured fields. Evidence for large variations in the PA of polarization vectors across the p profile is seen for IRAS 16342–3814, IRAS 17150–3224 and IRAS 1404–2713 at 1612 MHz. In these targets, however, the linearly polarized flux is quite weak (usually less than 0.5 Jy) and the width of p features is as narrow as 0.3 km s^{-1} .

4.4. Zeeman splitting

At 1612 MHz we found S-shaped features in the V spectra of IRAS 07331+0021 and IRAS 18266–1239 (Fig. 4). It is possible that they arise due to the Zeeman effect, which could be confirmed by high angular resolution observations. Assuming that for the σ components an average velocity splitting of 0.236 km s^{-1} is produced by a magnetic field of strength of 1 mG, the corresponding strength of magnetic field along the line of sight is $-1.07 \pm 0.24 \text{ mG}$ for IRAS 07331+0021 and $-2.57 \pm 0.14 \text{ mG}$ for IRAS 18266–1239. A negative sign indicates a field pointing towards the observer. These estimates are consistent with the field strengths measured in AGB stars and other PPN candidates (Szymczak et al. 1998; Bains et al. 2003a).

4.5. Depolarization

A reduced degree of polarization for bright I features is seen in some objects in the sample. Figure 5 shows the percentage linear polarization as a function of the normalized total flux density for 6 objects with p flux seen in at least 35 spectral channels at 1612 MHz. Decreasing trends are clearly visible for IRAS 17393–2727, IRAS 18276–1431

Table 2. The strongest polarized OH features in PPN candidates.

IRAS name	Line (MHz)	V_c (km s ⁻¹)	$m_c(\sigma)$ (%)	V_l (km s ⁻¹)	$m_L(\sigma)$ (%)	$\chi(\sigma)$ (°)
07331+0021	1612	32.3	5.0(1.1)	32.5	12.3(0.4)	-31.6(1.6)
07399-1435	1667	19.0	-2.7(0.2)	20.4	10.7(0.4)	54.2(2.4)
08005-2356	1612	-0.3	-37.0(1.5)	-0.4	51.3(5.1)	30.5(5.7)
16342-3814	1612	-7.3	-70.8(2.1)	-7.5	14.2(1.9)	-43.8(10.7)
	1667	9.8	13.8(1.6)	-4.2	26.5(4.0)	-61.8(13.0)
17150-3754	1612	-125.3	-84.2(6.3)			
17150-3224	1612	25.0	-5.2(0.8)	24.9	9.0(1.0)	79.8(2.4)
	1667	26.0	8.6(1.4)	25.9	4.2(0.4)	-68.2(5.6)
17253-2831	1612	-71.6	-2.9(0.3)			
17347-3139	1612	-23.1	11.9(2.4)			
17375-2759	1612	22.2	-7.1(2.6)	23.8	16.1(2.0)	-17.5(8.3)
17375-3000	1612	-35.6	-9.5(1.2)			
17385-3332	1612	-245.6	-7.0(2.3)	-224.3	4.1(1.1)	19.6(12.1)
17393-2727	1612	-120.5	12.9(0.8)	-123.5	4.2(0.2)	-60.8(3.3)
	1667	-124.5	-13.5(3.2)	-124.5	24.3(4.3)	6.6(13.8)
17393-3004	1612	16.1	-29.6(2.6)	-27.4	11.4(0.5)	-23.3(5.5)
	1667	-22.9	-38.7(20.5)			
17404-2713	1612	30.7	-6.6(0.4)	31.7	5.9(0.9)	57.0(4.2)
	1667	54.8	-24.9(5.5)	55.0	19.6(6.2)	-1.3(4.8)
17443-2949	1612	-15.4	-12.8(1.0)			
17579-3121	1612	-0.2	-9.3(1.1)	22.3	3.0(0.1)	-34.5(5.5)
18016-2743	1612	61.4	12.0(2.8)	61.4	15.9(2.7)	0.2(10.6)
18025-3906	1612	-129.1	23.1(3.0)			
18052-2016	1612	79.5	5.7(0.4)			
18071-1727	1612	17.6	17.0(0.7)			
18091-1815	1612	10.6	-5.4(7.0)			
	1667	8.3	32.4(4.7)	8.3	53.8(3.4)	-49.9(16.0)
18105-1935	1612	8.5	-7.0(0.4)			
18135-1456	1612	13.5	3.8(0.2)	13.1	5.1(0.2)	-21.2(3.8)
	1667	13.9	-7.6(0.6)			
18266-1239	1612	57.5	-2.6(0.5)	57.8	5.6(0.5)	71.9(4.3)
18276-1431	1612	73.3	-16.1(3.6)	48.8	3.5(0.1)	-69.8(6.0)
	1667	74.3	-15.4(1.3)	72.6	72.0(9.0)	80.4(7.0)
18450-0148	1612	40.5	11.3(1.8)	40.3	2.4(0.2)	63.3(5.2)
	1667	40.6	21.1(1.2)	26.4	19.0(2.4)	77.4(6.2)
18596+0315	1612	99.4	-11.0(2.4)	76.9	4.7(0.5)	-3.1(4.4)
19067+0811	1612	75.6	2.1(0.6)	76.5	69.9(18.9)	87.9(4.3)
19114+0002	1612	123.8	-6.5(0.2)	123.7	7.5(0.1)	-88.4(0.5)
	1612	124.9	-8.6(0.1)	124.9	1.8(0.1)	-86.9(2.6)
19219+0947	1612	-61.9	6.6(0.8)	-62.1	4.0(0.4)	3.9(10.0)
19255+2123	1612	21.2	-83.4(12.3)	21.3	39.9(10.1)	-57.2(22.7)
22036+5306	1612	-72.5	6.1(16.3)	-63.5	23.2(1.1)	-74.1(1.1)

and IRAS 19067+0811. The depolarization effect can be described by a power law of the form $m_L = AI^\alpha$ where $\alpha = -0.57 \pm 0.05$ effectively characterizes all the data for these three sources. This trend cannot be accounted for by the uncertainties in the fractional polarization. Observations of these

sources with different spectral resolutions (usually 0.07 or 0.14 km s⁻¹) have no significant influence on the decreasing trend. Sources IRAS 07331+0021, IRAS 18135-1456 and IRAS 19114+0002 do not show diminished polarization in spectral channels with high total intensities (Fig. 5). For the

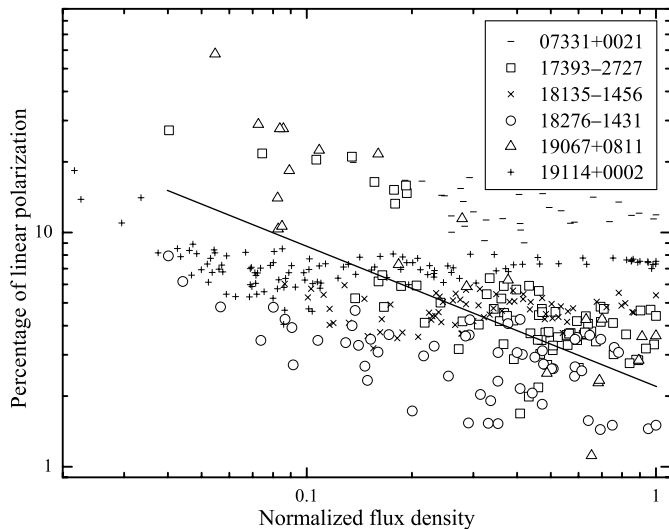


Fig. 5. Percentage of linear polarization versus the normalized total flux at 1612 MHz for sources with p flux higher than 5σ seen in more than 35 spectral channels. Each point represents data for channel of width 0.07 or 0.14 km s^{-1} , and 0.28 km s^{-1} for IRAS 19114+0002 (see Table 1). The line of slope of -0.57 is the best fit to the data marked by open symbols. Note the absence of decreasing trends for targets marked by small symbols.

remaining sources, the linearly polarized emission was detected in too few (3–25) channels to make a meaningful analysis of depolarization.

In looking for possible causes of depolarization it is worth noting that the extremely low dispersion (1.1 – 2.3) in the position angle of polarization vectors among the sources which do not show the depolarization effect, compared with 4.3 – 12.5 dispersion among the objects with depolarization (Fig. A.1). This suggests that the depolarization effect depends on the global magnetic field structure in the envelope; the directions of the projected field in the sources without depolarization are well aligned along specific PAs, whereas in the sources with depolarization the field geometry appears to be much more complex.

In the case of circularly polarized emission we note strong depolarization in IRAS 17393–2727 and IRAS 19067–0811. No depolarization is seen in IRAS 18276–1431 and in the other three sources not showing linear depolarization. This suggests that mechanisms for depolarization may be common to linear and circular emission.

4.6. Overshoot of 1667 MHz spectral extent

There are 20 objects with well detected blue- and red-shifted parts of spectra at 1612 and 1667 MHz (Table 1) and in 15 of them the spectral extent of the 1667 MHz line is by at least 0.2 km s^{-1} larger than that of the 1612 MHz line. All 7 objects with only the blue-shifted or red-shifted emission at one maser line (estimates of the presumed spectral extent are given in Table 1 as italic) but with the complete profile at other maser line also exhibit the overshoot of the 1667 MHz line relative to the 1612 MHz maser extent. The absolute value of overshoot usually ranges from 0.2 to 6 km s^{-1} . The distribution of the

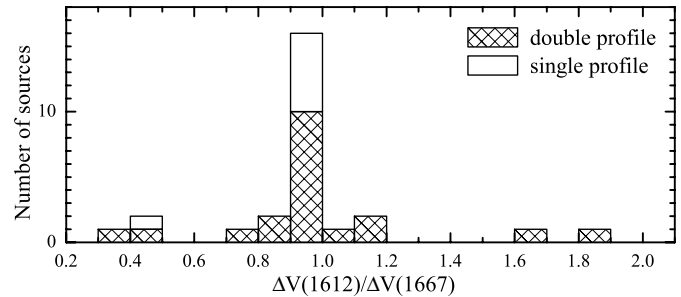


Fig. 6. Histogram of the ratio of the spectral maser extents at 1612 and 1667 MHz.

ratio of the velocity extent at 1612 and 1667 MHz is shown in Fig. 6. The overshoot effect is seen in 81% (22/27) of the objects in the sample.

The overshoot phenomenon is less prominent and less frequent (27–29%) in OH/IR objects (Dickinson & Turner 1991; Sivagnanam et al. 1989). Although there is no unique mechanism for overshoot (Sivagnanam & David 1999) a departure from spherical symmetry in the envelope is a plausible cause; most PPN candidates observed at high angular resolution show non-spherical geometry (Zijlstra et al. 2001).

4.7. Absorption features

We found 5 objects with absorption features, usually at 1667 MHz (Table 1). All these are inner Galaxy low latitude sources ($349^\circ < l < 13^\circ$, $|b| < 1.1^\circ$). In IRAS 17347–3139, IRAS 17393–3004 and IRAS 17443–2949 the velocities close to zero of the absorption features strongly suggest that they are interstellar in nature. OH maps by Boyce & Cohen (1994) confirm this unambiguously for the latter two objects. The absorption feature of IRAS 18091–1815 near 30.7 km s^{-1} appears in the red-shifted part of the OH spectrum and is possibly not related to the source. In IRAS 17103–3702 the 1667 MHz absorption near -37.8 km s^{-1} (see also Payne et al. 1988 and Zijlstra et al. 1989) coincides in velocity with the edge of the 1612 MHz maser emission. As only the blue-shifted emission is observed it is likely that the absorption arises in front of the ionized region of the nebula. This OH PPN object possibly represents an older phase of evolution. We conclude that in the studied sources, the OH absorption features are generally interstellar in origin.

5. Discussion

The present systematic data reveal an OH polarization pattern in PPN candidates which is quite different from that described in the literature for late-type stars. Out of 40 targets detected at 1612 MHz, 21 and 31 were found to show linearly and circularly polarized features, respectively. Early observations did not provide evidence for polarization in many PPNe, with the exception of a few stars during flare activities, (Cohen 1989, for a review). Considerable circular polarization was found in supergiants (Cohen et al. 1987) and OH/IR stars (Zell & Fix 1991) when observed with high sensitivity and spectral resolution. Zijlstra et al. (1989) measured circular polarization

in 5 PPN candidates and polarized emission was detected in IRAS 17150–3754 and IRAS 17393–2727.

Out of 34 1667 MHz objects, 9 exhibited linearly polarized emission. This detection ratio is about 2.5 times higher than that reported for Mira-type stars (Olnon et al. 1980; Claussen & Fix 1982). Because linearly polarized features are generally weak (0.5–4 Jy) and narrow (0.3–0.5 km s⁻¹) their only occasional detection in the past seems to be partly an effect of insufficient sensitivity and spectral resolution.

We note that at the two OH frequencies studied, linearly polarized features are always associated with circularly polarized features, but circular polarization can be present without associated linear polarization. A similar correlation has been reported for AGB stars (Claussen & Fix 1982). Appearance of circular polarization alone suggests that the effect of magnetic beaming (Gray & Field 1995) can work in the PPN objects.

5.1. Upper limit for electron density

In IRAS 18276–1431 and IRAS 19114+0002 linearly polarized features in the red-shifted parts of spectra at the two transitions were observed at the same velocities (Figs. 1 and A.1). Strong enough features (>0.5 Jy) at 1612 and 1667 MHz were identified in IRAS 18276–1431 near 72.8 and 74.4 km s⁻¹ and in IRAS 19114+0002 near 124.9 km s⁻¹. Assuming that both lines emerge in the same volume of gas, any difference in χ between the two lines would probably be due to Faraday rotation over the envelope path length. No significant differences in PA exist within errors of 9°9 and 12°4 for IRAS 18276–1431 and IRAS 19114+0002, respectively. As the radii of OH envelopes at the transitions of interest were determined in both targets (Bains et al. 2003a; Gledhill et al. 2001) and the strength of the magnetic field along the line of sight was measured in the first object (4.6 mG) we can estimate an upper limit of the mean electron density in the envelope from the expression for Faraday rotation (Garcia-Barreto et al. 1988):

$$\phi = 0.5n_e B_{\parallel} L \lambda^2, \quad (7)$$

where n_e is the electron density in cm⁻³, B_{\parallel} is the strength of magnetic field along the line of sight in mG, L is the depth of the maser region in units of 10¹⁵ cm and λ is the wavelength of the transition in units 18 cm. For an adopted distance of 2 kpc to OH17.7–2.0 (IRAS 18276–1431) the depth of the maser region is comparable with the diameter of the envelope of 5.1×10^{16} cm (Bains et al. 2003a). The radiation comes from the far side of the envelope. The above observational parameters of OH17.7–2.0 imply an upper limit for n_e of 1.2 cm⁻³. Such a low value suggests largely neutral matter in the envelope.

5.2. Magnetic fields in PPNe

Our polarimetric observations revealed a great variety of polarization properties of OH maser lines in PPNe. IRAS 19255+2123 is a good example to illustrate the diversity of polarization properties. The 1612 MHz emission is largely unpolarized with the exception of the feature near 21.2 km s⁻¹ which shows elliptical polarization ($m_C = -83\%$, $m_L = 40\%$).

We failed to detect any polarized emission at 1667 MHz. Considerable circular polarization at 1665 MHz was reported by Miranda et al. (2001). As the emission from both main lines is located in different parts of the envelope from the 1612-MHz emission it is likely that their polarization parameters are due to the local magnetic field strength and orientation. The 1612 MHz data imply that the PA of the projected magnetic field differs by 53° from the PA of the bipolar lobes observed in radio continuum (Miranda et al. 2001). This result partly supports the theoretical models of outflows in PNe collimated by toroidal magnetic fields (Garcia-Segura et al. 1999; Matt et al. 2000). However, the small number of polarized OH features in this source prevents the study of the magnetic field orientation with high angular resolution in order to verify the existence of a magnetized torus postulated by Miranda et al. (2001).

Although the magnetic field of 1–2 mG tentatively found in two PPN objects needs further confirmation by high angular resolution studies, its strength is consistent with that measured with MERLIN in IRAS 18276–1431 (Bains et al. 2003a) as well as in AGB stars (Szymczak et al. 1998). A simple consideration suggests that the magnetic field of the order of a few mG can shape the outflow in this object (Bains et al. 2003a). They document how IRAS 18276–1431 has a magnetic field with large-scale well ordered structure, the geometry of which is consistent with a stretched dipole. The signature of a structured field is seen in the polarization vector PA profile (Fig. 1). Several sources in our sample, most prominently IRAS 17393–2727, show clear evidence for a more complex magnetic field. Among the promising candidates is IRAS 19114+0002 which shows broad linearly polarized features at red-shifted velocities at both lines and much weaker blue-shifted features at 1612 MHz. The strongest linearly polarized features, near 124 km s⁻¹, are 2 and 7% of the total peak flux densities at 1667 and 1612 MHz, respectively. MERLIN observations of both lines failed to detect any polarized emission above the noise level (Gledhill et al. 2001) possibly due to insufficient spectral resolution. Our data show very small and smooth changes of the polarization position angles for the two lines, suggesting a magnetic field aligned along PA $\approx 5^\circ$. The distribution of the 1667 MHz emission is elongated along PA = 15° (Gledhill et al. 2001); suggesting that the magnetic field is well aligned approximately parallel to the possible outflow direction.

Three targets (including IRAS 19114+0002) possess OH spectra which are rich in linearly polarized features and do not exhibit the depolarization effect (shown by small symbols in Fig. 5). All these objects have highly aligned fields, as judged from the polarization position angle profiles. In contrast, the three sources with prominent depolarization (open symbols in Fig. 5) exhibit greater deviations in their linear polarization PAs across their velocity profiles. We suggest that they have structured magnetic fields of geometry similar to that observed in IRAS 18276–1431. We speculate that the weakly polarized emission from these bright sources is intrinsically polarized but has been depolarized in regions of complex magnetic field. Alternatively, intrinsically weakly or unpolarized emission due to the relationship between our viewing angle

Table 3. The p -flux-weighted average polarization angle of the linearly polarized OH maser emission at 1612 MHz and/or 1667 MHz (PA_{1612} , PA_{1667}) and the position angle of nebula long axis (PA_{axis}) taken from optical and/or infrared or radio images.

IRAS name	Type	N	$PA_{1612}(^{\circ})$	$\sigma_{PA_{1612}}(^{\circ})$	$PA_{1667}(^{\circ})$	$\sigma_{PA_{1667}}(^{\circ})$	$PA_{\text{axis}}(^{\circ})$	Refs.
07331+0021	d	3	-32.3	4.7			89(30)	1
07399-1435	c	4			48.0	6.7	23(5)	1, 2
08005-2356	s	2	22.1	4.4			-47(5)	3
16342-3814	d, d	4	-54.8	8.4	-51.6	5.6	69(3)	3
17150-3224	s, c	5	-72.2	32.9	-37.2	17.2	-33(3)	3
17393-3004	s	2	-23.0	6.5			13(3)	4
18266-1239	c	2	50.6	7.2			66(30)	5
18276-1431	c, c	1	47.0	5.0	77.0	14.8	20(3)	6
18450-0148	c, s	3	82.1	18.5	75.3	3.8	63(2)	7
19114+0002	c, c	2	-84.8	8.4	-84.0	7.3	21(3)	3
19219+0947	c	2	-0.7	4.5			34(5)	8
19255+2123	s	5	64.5	2.5			27(5)	9, 10
22036+5306	c	3	-73.8	5.3			66(2)	11

Type of spectrum: s – single peak, d – two features, c – complex; N : number of observations used to derive PA_{1612} and PA_{1667} ; references for PA_{axis} : (1) Meixner et al. (1999), (2) Kastner et al. (1998), (3) Ueta et al. (2000), (4) Philipp et al. (1999), (5) Chapman (1988), (6) Bains et al. (2003a), (7) Imai et al. (2002), (8) Seaquist & Davis (1983), (9) Miranda et al. (2000), (10) Miranda et al. (2001), (11) Sahai et al. (2003).

and the source magnetic field configuration and maser beaming effects (Gray & Field 1995; Elitzur 1996, 1998) becomes polarized with the PA varying steeply as a function of angular position and apparent velocity. As pointed out in Sect. 5.1 the Faraday rotation in these objects is probably too small to affect the detectability of linear polarization.

5.3. Prevalence of orthogonal fields

These single dish measurements of the polarization position angle of OH masers provide useful information on the orientation of the magnetic field in the maser region. It has been commonly argued that features with linear polarization are σ components of the Zeeman pattern (Garcia-Barreto et al. 1988; Gray & Field 1995; Szymczak et al. 1998), implying that the projected angle of the magnetic field on the plane of the sky is perpendicular to the polarization position angle. Several objects in the sample have been imaged in the optical and/or infrared showing axisymmetric morphology. 13 of them exhibit linearly polarized OH maser emission, so that one can compare the position angle of the magnetic field with that of the outflow axis. The p -flux-weighted average polarization angles for these sources are given in Table 3 for one or two OH lines together with the position angle of the long axis of the nebula taken from the literature. A plot of the PA of the mean magnetic field versus the PA of the long axis of the nebula (Fig. 7) shows a scarcity of objects with the magnetic field aligned with the outflow. The distribution of the absolute difference in PA between nebula and magnetic field axes is clearly skewed; the median value of this distribution is 52° . Thus, the magnetic field is closer to orthogonal than parallel direction relative to the long axis although there is a large scatter.

The dominance of magnetic field components oriented across the outflow axis appears to support the hypothesis

of magnetic collimation of bipolar lobes or jets (Chevalier & Luo 1994; Garcia-Segura et al. 1999; Matt et al. 2000). In this model the initially weak magnetic fields emerging from an AGB star are wrapped up by differential rotation into toroidal tubes which channel the fast wind in post-AGB phase producing prolate and bipolar structures. Recent observations provided arguments for toroidal fields in individual PN and PPN (Greaves 2002; Miranda et al. 2001). Alternatively, prevalence of the orthogonal field can be related to the source geometry. It is known that OH masers in PPNe are preferentially seen along the limbs of biconical outflows (Zijlstra et al. 2001). For sources with the opening angle wide enough the PA of the magnetic field in the maser regions could be misaligned with the nebula long axis.

5.4. Disappearance of OH masers

No OH emission was detected in 5 targets (Table 1). In IRAS 06530-0213 weak 1667 MHz emission (0.22 and 0.16 Jy) at 27.8 and 29.8 km s^{-1} was observed in 1986 and 1987 (Likkel 1989). No 1612 MHz emission was detected (Likkel 1989; Hu et al. 1994). The source was classified recently as a carbon-rich PPN (Hrivnak & Bacham 2003). IRAS 16559-2957 was detected at 1612 MHz in 1986 with a 0.58 Jy peak near 56.2 km s^{-1} (Likkel 1989). At a similar epoch te Lintel Hekkert et al. (1991) observed the blue-shifted emission at 57.0 km s^{-1} (0.43 Jy) and red-shifted emission at 86.5 km s^{-1} (0.15 Jy), while in 1991 Hu et al. (1994) found a 0.30 Jy peak near about 70 km s^{-1} at 1612 and 1665 MHz. In IRAS 17079-3844 a 1612 MHz multi-peak profile was seen in 1987 (te Lintel Hekkert et al. 1991). The 1667 MHz maser from IRAS 17436+5003 was found by Likkel (1989) in 1986 and 1987 near a velocity of -26 km s^{-1} . Recent observations by Bains et al. (2003b) suggest that the

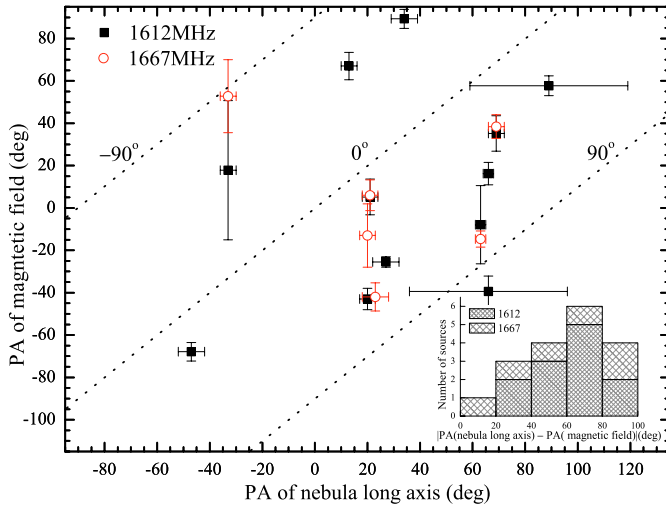


Fig. 7. Position angle of the magnetic field vector versus position angle of the long axis of the nebula. Squares and circles mark the 1612 and 1667 MHz masers respectively. The diagonal dotted lines correspond to constant differences of -90° , 0° and 90° between the two position angles. The inset shows the distribution of the absolute difference in PA.

disappearance of OH maser in this source can be permanent. In IRAS 19127+1717, 1667 MHz emission was detected at 15.6 km s^{-1} (0.24 Jy) in 1987 (Likkel 1989). She suggested that the emission is probably not related to the nebula.

We point out that all 5 targets not detected in the survey were known as weak ($0.2\text{--}0.4 \text{ Jy}$) OH emitters about 15–17 years ago. Their emission has dropped below $\sim 0.1 \text{ Jy}$. These objects need further observations to decide whether the emission disappeared temporarily or permanently.

One of the most interesting objects in the sample IRAS 17393–2727 (OH0.9+1.3) continues to show a growth of the blue-shifted emission at a rate of about 1 Jy yr^{-1} (Shepherd et al. 1990), whereas its red-shifted emission near -93.5 km s^{-1} appears to be constant, within a 0.2 Jy accuracy, as compared to Shepherd’s data taken about 14 yrs ago.

6. Conclusions

High sensitivity observations of the 1612 and 1667 MHz OH masers from a sample of 47 proto-planetary nebula candidates have provided new information on the polarization pattern.

A large fraction (55%) of the sources exhibit linearly polarized features in one or both OH lines. Circularly polarized features are present in 76% of the sources. Generally the maser features are elliptically polarized; the degrees of linear and circular polarization are usually low ($<15\%$), but in some features this is as high as 50–80%. The linearly polarized features are usually narrow ($<0.5 \text{ km s}^{-1}$) and weak ($<4 \text{ Jy}$).

There are several sources with a large velocity extent ($>4 \text{ km s}^{-1}$) of linearly polarized flux for which a diversity of variations of polarization position angle χ across the profile is observed. The sources with large changes in χ are very likely to have structured magnetic fields, as recently revealed for OH17.7–2.0. They also exhibit depolarization of linearly

polarized emission. The sources with nearly constant values of χ possibly have magnetic fields highly aligned with specific directions and do not show depolarization effects. Both types of objects appear to be good candidates for future mapping of magnetic fields with high angular and spectral resolutions.

For the subset of PPNe with optical images showing axisymmetric morphology we found a dominance of magnetic field components misaligned by $>60^\circ$ with the long axis of the nebulae. This finding lends support to the theoretical model of magnetic collimation of bipolar lobes in planetary nebulae.

The magnetic field strength inferred from likely Zeeman pairs detected in two targets is of the order of 1–2 mG; a value which is consistent with previous estimates for PPN and AGB stars. The upper limit of the electron density of 1 cm^{-1} in OH17.7–2.0 derived from a comparison of χ angles at 1612 and 1667 MHz lines implies a largely neutral envelope.

The overshoot of the 1667 MHz velocity extent relative to the 1612 MHz velocity extent is common (81%) in the studied sources. This effect, rarely seen in AGB stars, can be related to changes in the source geometry and excitation conditions in the envelopes during the transition from AGB to PN phase.

Acknowledgements. We thank A. Richards for useful comments on an earlier version of this paper, P. Colom for the communication of his results of polarization measurements of the NRT prior to publication. The Nançay Radio Observatory is the Unité Scientifique de Nançay of the Observatoire de Paris, associated with the CNRS. The Nançay Observatory gratefully acknowledges the financial support of the Region Centre in France.

References

- Bains, I., Gledhill, T. M., Yates, J. A., & Richards, A. M. S. 2003a, MNRAS, 338, 287
- Bains, I., Yates, J. A., Gledhill, T. M., & Richards, A. M. S. 2003b, MNRAS, 346, L46
- Balick, B., & Frank, A. 2002, ARA&A, 40, 439
- Boyce, P. J., & Cohen, R. J. 1994, A&AS, 107, 563
- Bridle, A. H., Davis, M. M., Fomalont, E. B., & Lequeux, J. 1972, AJ, 77, 6
- Chapman, J. M. 1988, MNRAS, 230, 415
- Chevalier, R., & Luo, D. 1994, ApJ, 421, 225
- Claussen, M. J., & Fix, J. D. 1982, ApJ, 263, 153
- Cohen, R. J. 1989, Rep. Prog. Phys., 52, 881
- Cohen, R. J., Downs, G., Emerson, R., et al. 1987, MNRAS, 225, 491
- Dickinson, D. J., & Turner, B. E. 1991, ApJS, 75, 1323
- Elitzur, M. 1996, ApJ, 457, 415
- Elitzur, M. 1998, ApJ, 504, 390
- Garcia-Barreto, J. A., Burke, B. F., Reid, M. J., et al. 1988, ApJ, 326, 954
- Garcia-Segura, G., Langer, N., Rózycka, M., & Franco, J. 1999, ApJ, 517, 767
- Gledhill, T. M., Yates, J. A., & Richards, A. M. S. 2001, MNRAS, 328, 301
- Gray, M. D., & Field, D. 1995, A&A, 298, 243
- Greaves, J. S. 2002, A&A, 392, L1
- Habing, H. J. 1996, A&AR, 7, 97
- Hrivnak, B. J., & Bacham, E. R. 2003, ApJ, 590, 1049
- Hu, J. Y., te Lintel Hekkert, P., Slijkhuis, S., et al. 1994, A&AS, 103, 301
- Imai, H., Obara, K., Diamond, P. J., Omodaka, T., & Sasao, T. 2002, Nature, 417, 829

- Kastner, J. H., Weintraub, D. A., Merrill, K. M., & Gatley, I. 1998, *AJ*, 116, 1412
- Kemball, A. J., & Diamond, P. J. 1997, *ApJ*, 481, L111
- Kwok, S. 1993, *ARA&A*, 31, 63
- Likkel, L. 1989, *ApJ*, 344, 350
- Matt, S., Balick, B., Winglee, R., & Goodson, A. 2000, *ApJ*, 545, 965
- McIntosh, G. C., & Predmore, C. R. 1993, *ApJ*, 404, L71
- Meixner, M., Ueta, T., Dayal, A., et al. 1999, *ApJS*, 122, 221
- Miranda, L. F., Fernandez, M., Alcalá, J. M., et al. 2000, *MNRAS*, 311, 748
- Miranda, L. F., Gomez, Y., Anglada, G., & Torrelles, J. M. 2001, *Nature*, 414, 284
- Olson, F. M., Winnberg, A., Matthews, H. E., & Schultz, G. V. 1980, *A&AS*, 42, 119
- Payne, H. E., Phillips, J. A., & Terzian, Y. 1988, *ApJ*, 326, 368
- Philipp, S., Tuffs, R. J., Mezger, P. G., & Zylka, R. 1999, *A&A*, 350, 582
- Sahai, R., Zijlstra, A., Sanchez Contreras, C., & Morris, M. 2003, *ApJ*, 586, L81
- Seaquist, E. R., & Davis, L. E. 1983, *ApJ*, 274, 659
- Shepherd, M. C., Cohen, R. J., Gaylard, M. J., & West, M. E. 1990, *Nature*, 344, 522
- Sivagnanam, P., & David, P. 1999, *MNRAS*, 304, 622
- Sivagnanam, P., Le Squeren, A. M., Foy, F., & Minh, F. T. 1989, *A&A*, 211, 341
- Soker, N. 2002, *MNRAS*, 336, 826
- Szymczak, M., & Cohen, R. J. 1997, *MNRAS*, 288, 945
- Szymczak, M., Cohen, R. J., & Richards, A. M. S. 1998, *MNRAS*, 297, 1151
- Szymczak, M., Cohen, R. J., & Richards, A. M. S. 2001, *A&A*, 371, 1012
- te Lintel Hekkert, P. 1991, *A&A*, 248, 209
- te Lintel Hekkert, P., & Chapman, J. M. 1996, *A&AS*, 119, 459
- te Lintel Hekkert, P., Caswell, J. L., Habing, H. J., Haynes, R. F., & Norris, R. P. 1991, *A&AS*, 90, 327
- Ueta, T., Meixner, M., & Bobrowsky, M. 2000, *ApJ*, 528, 861
- van Driel, W., Pezzani, J., & Gérard, E. 1996, in *High sensitivity radio astronomy*, ed. N. Jackson, & R. J. Davis (Cambridge Univ. Press), 229
- Wardle, J. F. C., & Kronberg, P. P. 1974, *ApJ*, 194, 249
- Zell, P. J., & Fix, J. D. 1991, *ApJ*, 369, 506
- Zijlstra, A. A., te Lintel Hekkert, P., Pottasch, S. R., et al. 1989, *A&A*, 217, 157
- Zijlstra, A. A., Chapman, J. M., te Lintel Hekkert, P., et al. 2001, *MNRAS*, 322, 280

Online Material

Appendix A: Full polarization spectra

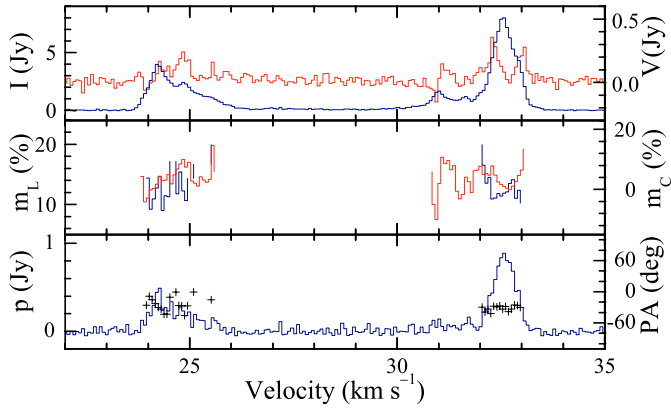


Fig. A.1. Same as in Fig. 1 for the 1612 MHz transition in IRAS 07331+0021 taken on 2002, July 5.

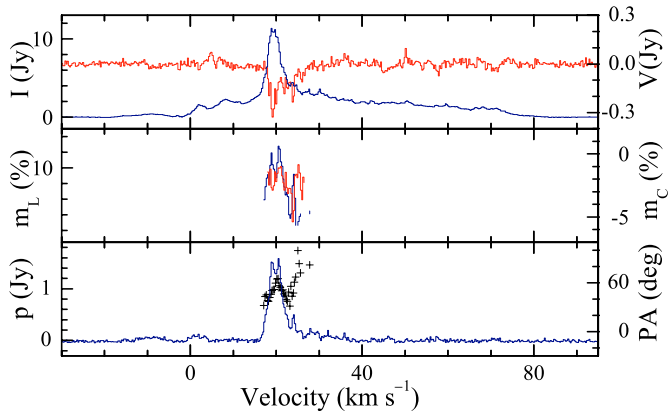


Fig. A.2. Same as in Fig. 1 for the 1667 MHz transition in IRAS 07399-1435 taken on 2002, June 16.

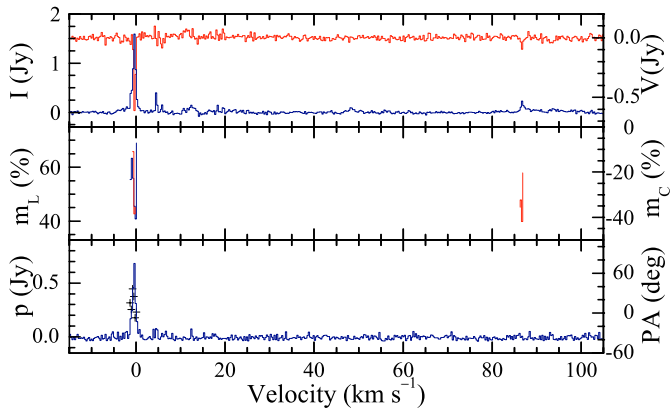


Fig. A.3. Same as in Fig. 1 for the 1612 MHz transition in IRAS 08005-2356 taken on 2002, May 15.

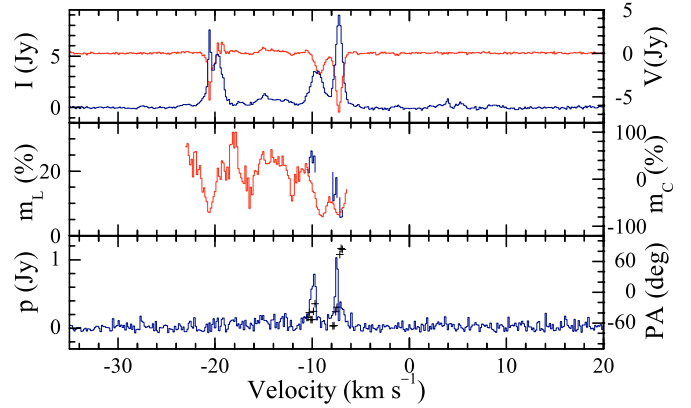


Fig. A.4. Same as in Fig. 1 for the 1612 MHz transition in IRAS 16342-3814 taken on 2003, April 28. There is not linearly polarized emission at the red-shifted part of the spectrum and only the blue-shifted part is shown.

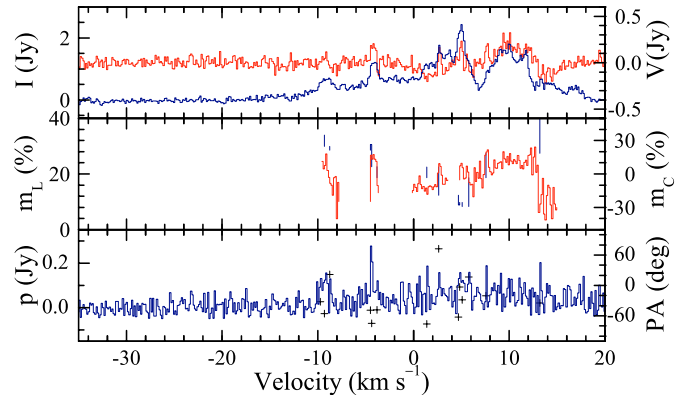


Fig. A.5. Same as in Fig. 1 for the 1667 MHz transition in IRAS 16342-3814 taken on 2003, April 28. There is not linearly polarized emission at the red-shifted part of the spectrum and only the blue-shifted part is shown.

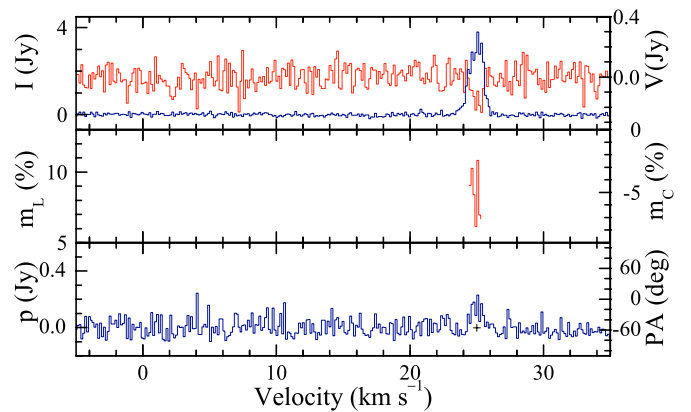


Fig. A.6. Same as in Fig. 1 for the 1612 MHz transition in IRAS 17150-3224 taken on 2003, March 19.

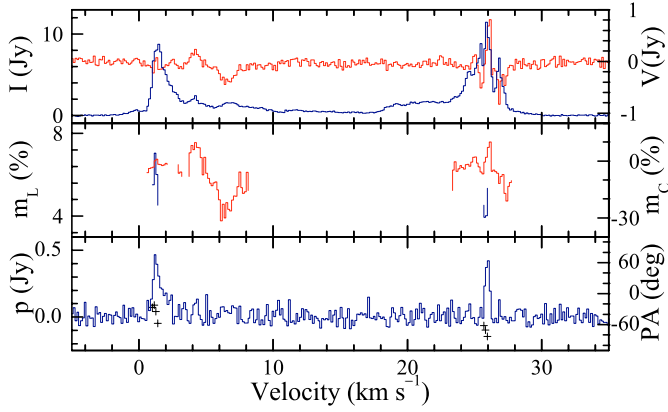


Fig.A.7. Same as in Fig. 1 for the 1667 MHz transition in IRAS 17150–3224 taken on 2003, March 19.

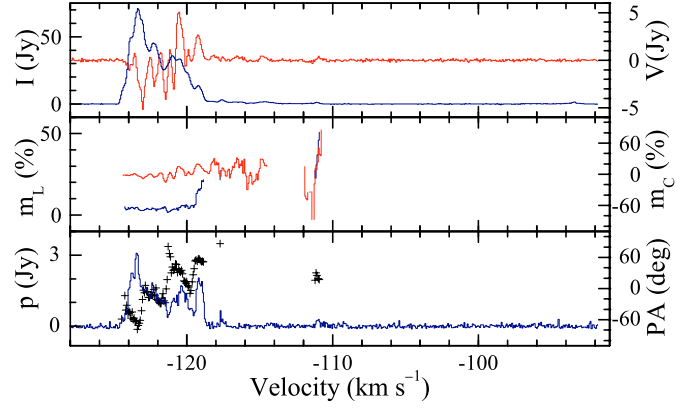


Fig.A.10. Same as in Fig. 1 for the 1612 MHz transition in IRAS 17393–2727 taken on 2003, February 1.

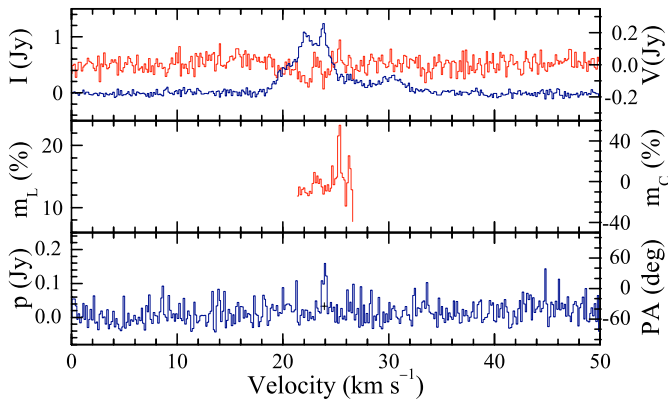


Fig.A.8. Same as in Fig. 1 for the 1612 MHz transition in IRAS 17375–2759 taken on 2003, June 27.

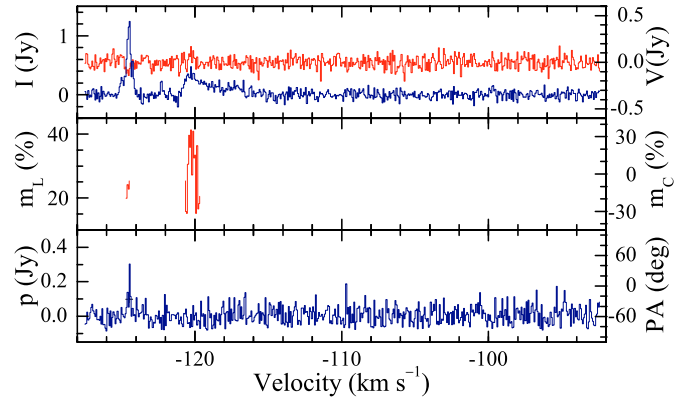


Fig.A.11. Same as in Fig. 1 for the 1667 MHz transition in IRAS 17393–2727 taken on 2003, February 1.

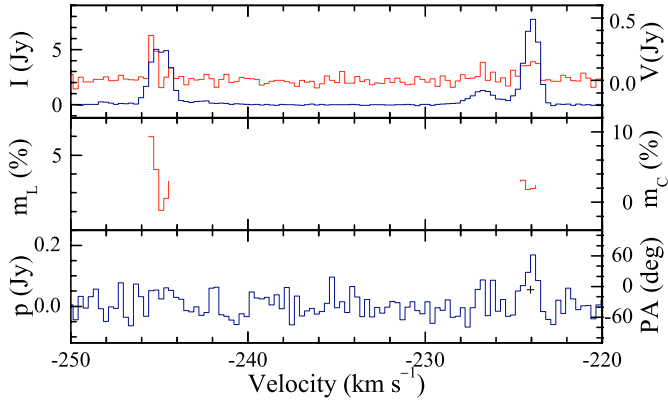


Fig.A.9. Same as in Fig. 1 for the 1612 MHz transition in IRAS 17385–3332 taken on 2002, September 12.

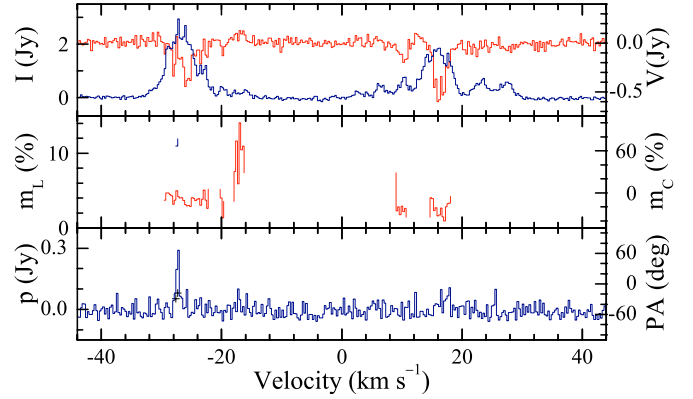


Fig.A.12. Same as in Fig. 1 for the 1612 MHz transition in IRAS 17393–3004 taken on 2003, June 30.

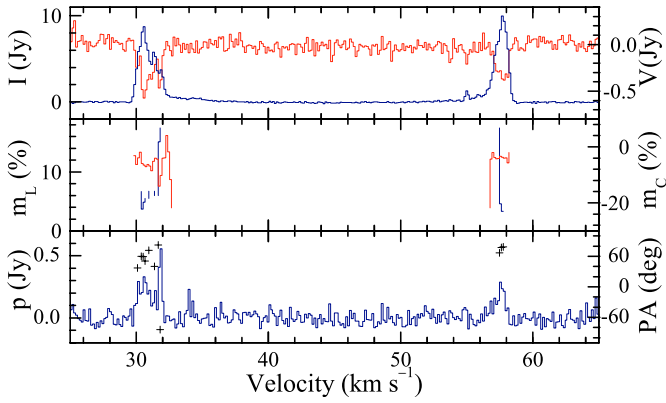


Fig.A.13. Same as in Fig. 1 for the 1612 MHz transition in IRAS 17404–2713 taken on 2003, February 1.

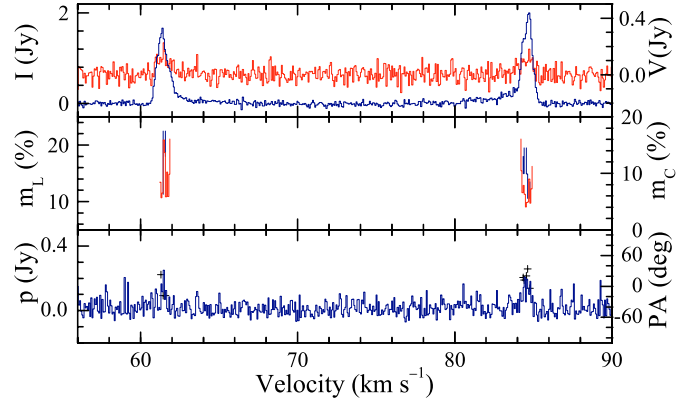


Fig.A.16. Same as in Fig. 1 for the 1612 MHz transition in IRAS 18016–2743 taken on 2002, May 24.

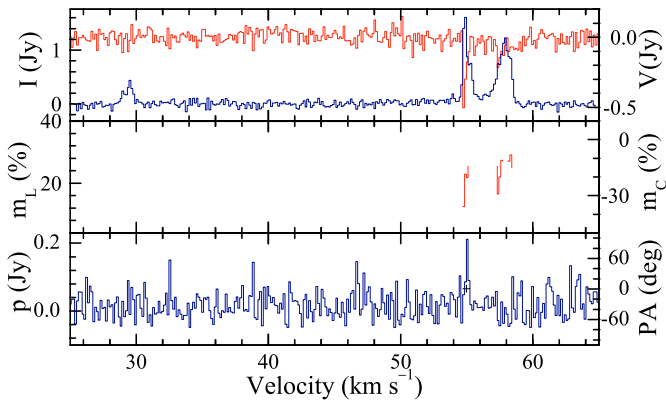


Fig.A.14. Same as in Fig. 1 for the 1667 MHz transition in IRAS 17404–2713 taken on 2003, February 1.

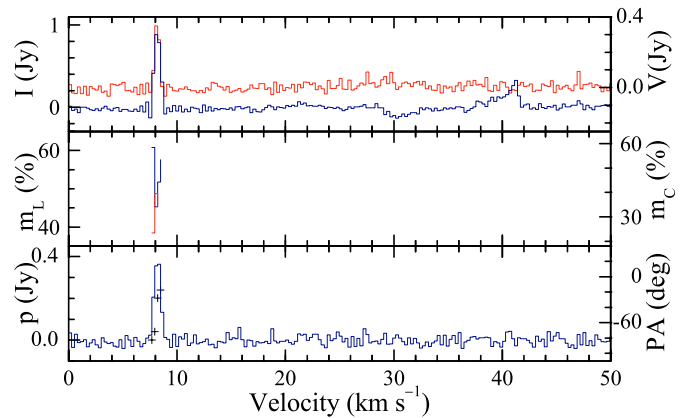


Fig.A.17. Same as in Fig. 1 for the 1667 MHz transition in IRAS 18091–1815 taken on 2002, June 10.

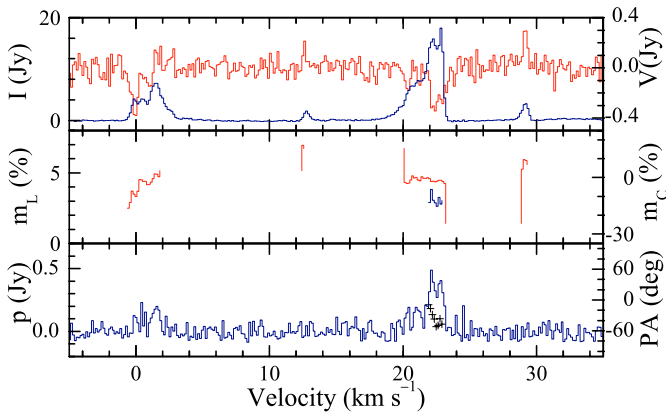


Fig.A.15. Same as in Fig. 1 for the 1612 MHz transition in IRAS 17579–3121 taken on 2003, February 12.

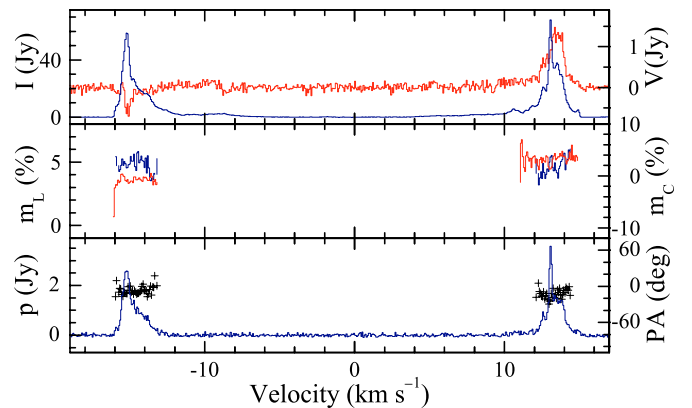


Fig.A.18. Same as in Fig. 1 for the 1612 MHz transition in IRAS 18135–1456 taken on 2003, February 23.

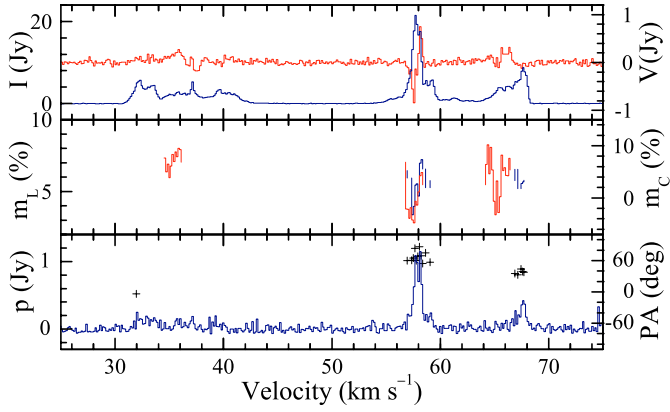


Fig.A.19. Same as in Fig. 1 for the 1612 MHz transition in IRAS 18266–1239 taken on 2002, August 12.

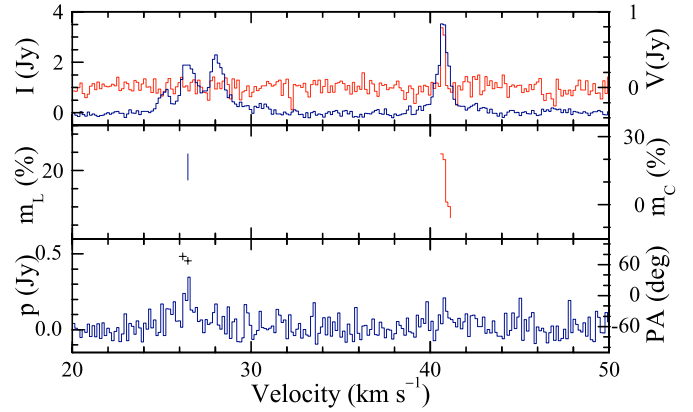


Fig.A.22. Same as in Fig. 1 for the 1667 MHz transition in IRAS 18450–0148 taken on 2003, May 17.

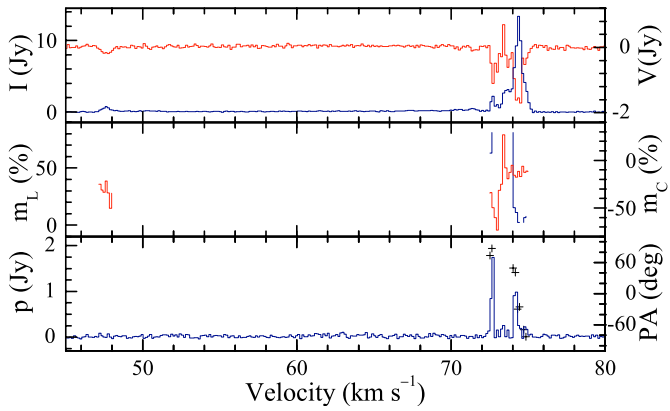


Fig.A.20. Same as in Fig. 1 for the 1667 MHz transition in IRAS 18276–1431 taken on 2002, February 20.

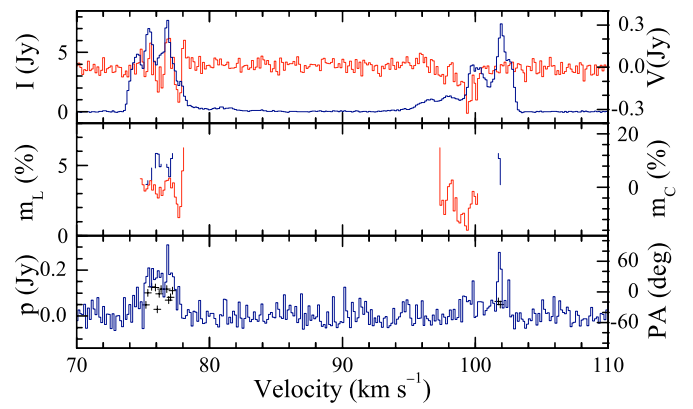


Fig.A.23. Same as in Fig. 1 for the 1667 MHz transition in IRAS 18596+0315 taken on 2002, June 4.

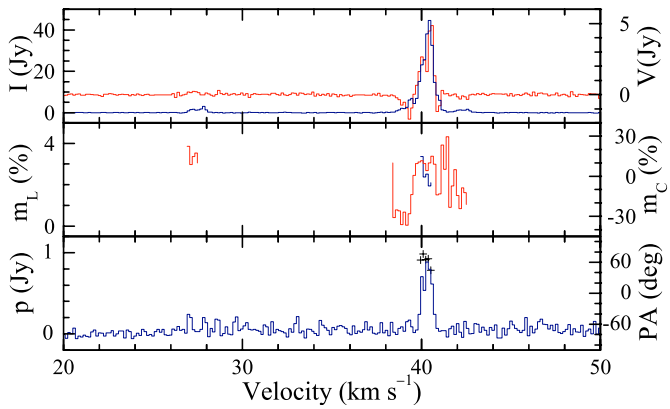


Fig.A.21. Same as in Fig. 1 for the 1612 MHz transition in IRAS 18450–0148 taken on 2003, May 17.

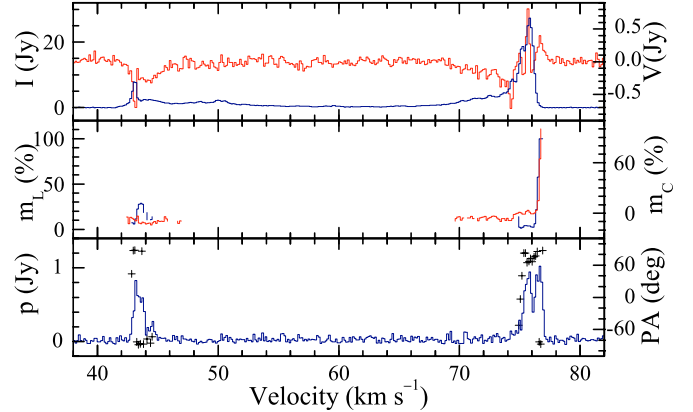


Fig.A.24. Same as in Fig. 1 for the 1612 MHz transition in IRAS 19067+0811 taken on 2003, February 23.

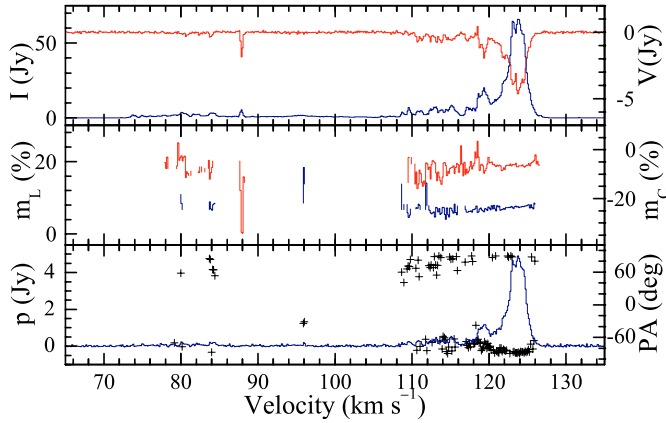


Fig. A.25. Same as in Fig. 1 for the 1612 MHz transition in IRAS 19114+0002 taken on 2003, June 18.

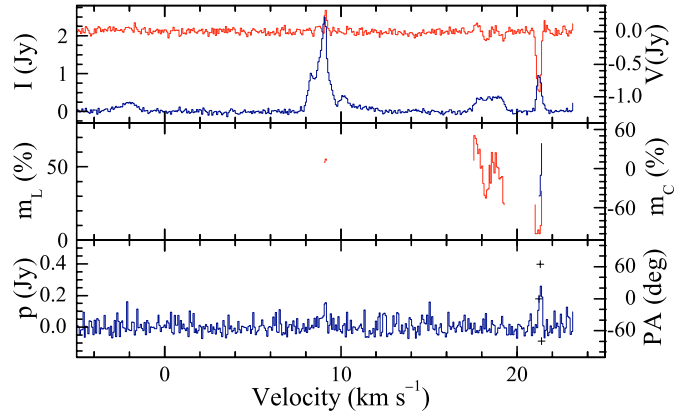


Fig. A.28. Same as in Fig. 1 for the 1612 MHz transition in IRAS 19255+2123 taken on 2002, May 25.

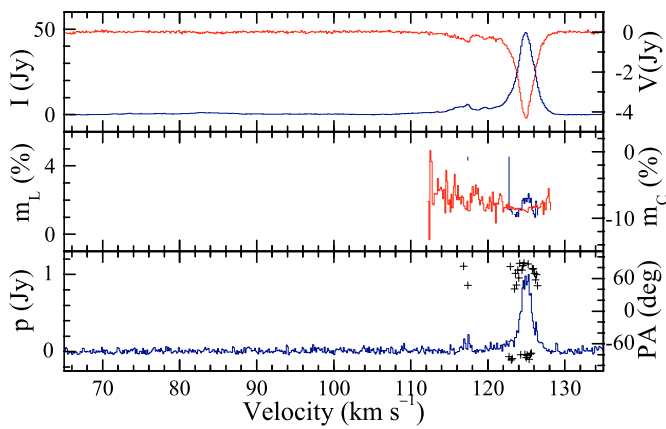


Fig. A.26. Same as in Fig. 1 for the 1667 MHz transition in IRAS 19114+0002 taken on 2003, June 18.

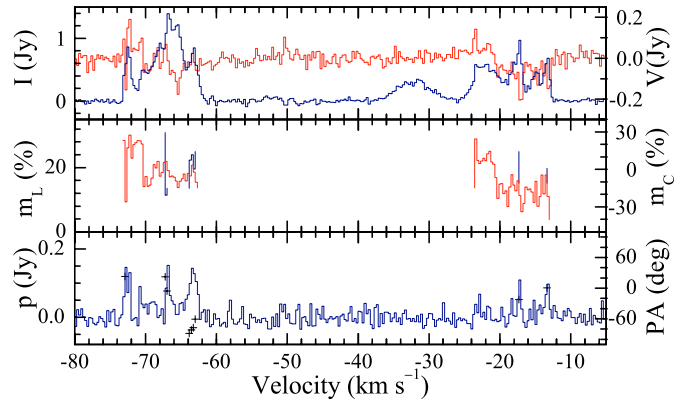


Fig. A.29. Same as in Fig. 1 for the 1612 MHz transition in IRAS 22036+5306 taken on 2002, March 1.

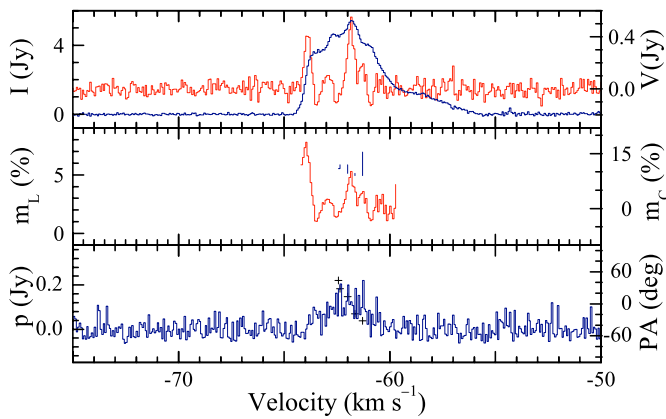


Fig. A.27. Same as in Fig. 1 for the 1612 MHz transition in IRAS 19219+0947 taken on 2003, May 15.